Chemosphere 313 (2023) 137421

Contents lists available at ScienceDirect

Chemosphere

journal homepage: www.elsevier.com/locate/chemosphere

In-situ construction of binder-free MnO_2/MnSe heterostructure membrane for high-performance energy storage in pseudocapacitors

Qasim Abbas [a], Abdul Mateen [b], Sajid Hussain Siyal [c], Najam Ul Hassan [d], Asma A. Alothman [e], Mohamed Ouladsmane [e], Sayed M. Eldin [f], Mohd Zahid Ansari [g,**], Muhammad Sufyan Javed [h,*]

[a] Department of Intelligent Manufacturing, Yibin University, Yibin, Sichuan, 644000, PR China
[b] Department of Physics and Beijing Key Laboratory of Energy Conversion and Storage Materials, Beijing Normal University, Beijing, 100084, China
[c] Metallurgy & Materials Engineering Department, Dawood University of Engineering and Technology, Karachi, 74800, Pakistan
[d] Department of Physics, Division of Science and Technology, University of Education, Lahore, 54000, Pakistan
[e] Department of Chemistry, College of Science, King Saud University, Riyadh, 11451, Saudi Arabia
[f] Faculty of Engineering and Technology, Future University in Egypt, New Cairo, 11835, Egypt
[g] School of Materials Science and Engineering, Yeungnam University, Gyeongsan, 712749, South Korea
[h] School of Physical Science and Technology, Lanzhou University, Lanzhou, 730000, China

HIGHLIGHTS

- Binder-free heterostructured MnO_2/MnSe-NR@CC are directly synthesized on the carbon cloth substrate.
- The MnO_2/MnSe-NR@CC electrode exhibits a maximum specific capacitance of 740.63 F/g at a current density of 1.5 A/g, with excellent capacitance retention of 93% up to 5000 cycles.
- The MnO_2/MnSe-NR@CC//AC-ASC delivered a maximum capacitance of 166.66 F/g at 2 A/g with outstanding capacitance retention of 93% after GCD 5000 cycles.
- The MnO_2/MnSe-NR@CC//AC-ASC delivers an energy density of 75.06 Wh/kg at 1805.1 W/kg and maintains 55.044 Wh/kg at a maximum power density of 18,159 W/kg.

GRAPHICAL ABSTRACT

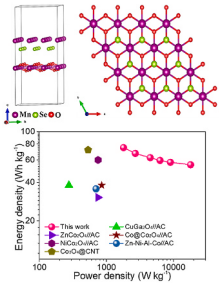

ARTICLE INFO

Keywords:
MnO_2
Heterostructure
Selenium
Positive electrode
Supercapacitor

ABSTRACT

Manganese (Mn)-based oxides are considered suitable positive electrode materials for supercapacitors (SCs). However, their cycle stability and specific capacitance are significantly hindered by key restrictions such as structural instability and low conductivity. Herein, we demonstrated a novel nanorod (NR)-shaped heterostructured manganese dioxide/manganese selenide membrane (MnO_2/MnSe) on carbon cloth (CC) (denoted as MnO_2/MnSe-NR@CC) with a high aspect ratio by a straightforward and facile hydrothermal process. Experiments have demonstrated that doping selenium atoms to oxygen sites reduce electronegativity, increasing the intrinsic electronic conductivity of MnO_2, decreasing electrostatic interactions with electrolyte ions, and thus

* Corresponding author. School of Physical Science and Technology, Lanzhou University, Lanzhou, China
** Corresponding author.
E-mail addresses: zahid.smr@yu.ac.kr (M.Z. Ansari), safisabri@gmail.com (M.S. Javed).

https://doi.org/10.1016/j.chemosphere.2022.137421
Received 21 September 2022; Received in revised form 11 November 2022; Accepted 26 November 2022
Available online 28 November 2022

boosting the reaction kinetics. Further, the selenium doping results in an amorphous surface with extensive oxygen defects, which contributed to the emergence of additional charge storage sites with pseudocapacitive characteristics. As expected, novel heterostructured MnO_2/MnSe-NR@CC as an electrode for SC exhibits a high capacitance of 740.63 F/g at a current density of 1.5 A/g, with excellent cycling performance (93% capacitance retention after 5000 cycles). The MnO_2/MnSe-NR@CC exhibited outstanding charge storage capability, dominating capacitive charge storage (84.6% capacitive at 6 mV/s). To examine the practical applications of MnO_2/MnSe-NR@CC-ASC as a positive electrode, MnO_2/MnSe-NR@CC//AC device was fabricated. The MnO_2/MnSe-NR@CC//AC-ASC device performed exceptionally well, with a maximum capacitance of 166.66 F/g at 2 A/g, with a capacitance retention of 94%, after 500 GCD cycles. Additionally, it delivers an energy density of 75.06 Wh/kg at a power density of 1805.1 W/kg and maintains 55.044 Wh/kg at a maximum power density of 18,159 W/kg. This research sheds fresh information on the anionic doping method and has the potential to be applied to the synthesis of positive electrode materials for energy storage applications.

1. Introduction

Sustainable and renewable energy storage systems are strongly in demand due to emerging trends of energy transformation and environmental safety. A great emphasis is put on the high performance of energy storage systems (Wan et al., 2022; Zhao et al., 2022). Rechargeable batteries and supercapacitors (SCs) are among those systems working on electrochemical energy storage mechanisms and are prevailing almost everywhere. SCs exhibit a fast charging-discharging process, low maintenance cost, longer life cycle, and stability (Zhao et al., 2020; Guo et al., 2019; Javed et al., 2022). Electrode materials play an obvious part in fabricating SCs, regardless of the charge storage mechanism involved. Lately, two schemes have been successful and often employed to achieve high-performance electrode materials having good porosity with multiple redox states for high electrochemical performance and augmented electrical conductivity. The first one endows high enough charge-transfer kinetics to electrode materials, delivering enough electrons to active materials, enabling them to fully use their storage capability, which leads to increased power density and energy density (Zhang et al., 2018).

These exquisite characteristics can be modified while considering the SCs making materials, e.g., electrodes or electrode forming materials. Transition metal oxides having variable valence, such as MnO_2 (Majumdar, 2021), Co_3O_4 (Mateen et al., 2022), Fe_3O_4 (Khan et al., 2020; Javed et al., 2021a), have been studied as prospective substitute materials as electrode materials for SC. Among them, MnO_2 owes a distinction due to its ease of access to the market, inexpensiveness, direct utilization, and nature friendliness. MnO_2-based electrodes have high specific capacitance; however, due to high electrical resistivity in strong current regimes, the specific capacitance value is substantially lowered, reducing the performance and cycle stability of the SC. Reversible Mn^{3+}/Mn^{4+} reaction originates large theoretical capacity making MnO_2 a choice of eminence at high working voltage. Such as, an excellent capacitance of 360.5 F/g at 1 A/g has been achieved by a MnO_2 nanosheets-carbon cloth-based electrode material (Long et al., 2020). Further, Gao et al. inserted oxygen vacancy into MnO_2 nanorod arrays by annealing in an H_2 environment, which successfully enhanced the conductivity and yielded a capacitance of 874.5 F/g at a current density of 0.25 A/g (Qiu and XiaoH. J. J. o. P. S. Gao, 2021). Wang et al. used substitutional doping to modify MnO_2 nanosheets, and then they built these modified nanosheets into high performance printable solid-state micro-SCs (Wang et al., 2020a). Nevertheless, the insufficient electrical conductivity of MnO_2 hinders the way to an ultra-prime performance of SCs. On the other hand, transition metal chalcogenides have a lower energy density, which prevents them from being used in applications requiring better performance (Sahoo et al., 2018; Miao et al., 2021; Javed et al., 2020). Its charge storage mechanism induces lower energy density based on redox reactions or ions adsorption on the surface layer (Javed et al., 2020; Yang et al., 2017a). A normal charge-discharge process is triggered by only a fraction of molecules leading to ionic or electronic transportation, preventing rapid faradaic reduction in bulk materials and kinetic oxidation processes (Salunkhe et al., 2017). Recent research focus has been diverted to improving the performance of SCs having high charge-discharge rates. The most commonly employed approach is either to enlarge the surface area or to minimize the charge-transfer resistance, in some cases, a combination of both (Dinesh et al., 2020; Yumak et al., 2019; Azman et al., 2019).

Carbon-based materials have been paid attention to lowering charge-transfer resistance (Zhai et al., 2011; Wang et al., 2012). Carbon cloth (CC) outperforms its counterparts due to its softness, mechanical strength, and flexibility for direct growth of nanomaterials (Shen et al., 2013; Shah et al., 2018a). The process implies a simple technique of coating/depositing active materials on CC and later using them as an electrode in SCs. In ideal circumstances, swift charge transfer and efficient ionic transportation should be there in the electrode's reaction kinetics, which is directly attributed to the electrode material's intrinsic structure.

Selenium (Se)-based materials have attracted great interest for fuel-cell catalysts, hydrogen evolution and storage, batteries, and supercapacitors (Arul and Han, 2016; Chen et al., 2015). Compared to oxygen and sulfur, selenium possesses greater metallic and electrical properties. The electrical conductivity of Se (1×10^{-3} S/m) is significantly higher than that of sulfur (5×10^{-28} S/m) (Nagaraju et al., 2017). Furthermore, Se demonstrates superior supercapacitive characteristics than sulfur (Gao et al., 2017). Metal selenides have recently received extensive attention as electrode materials for SCs with good performance and stability (Sakthivel et al., 2019). Among metal selenides, manganese selenide has attracted less attention recently (Sahoo et al., 2018). The vast majority of earlier reports indicated the synthesis of MnSe and its implementation in magneto-optical devices and solar cells (Yang et al., 2017b), but relatively few investigations were carried out to investigate its potential in energy storage (Balamuralitharan et al., 2017; Tang et al., 2018). A heterostructure composed of MnO_2/MnSe is the best option for enhancing the overall performance of SCs. The composite heterointerface interaction takes place between MnO_2 and MnSe in a heterostructure enables an increase in both interfacial electron transport and overall structural strength. This, in turn, results in an outstanding capacitance at relatively high current density, which is due to the synergistic influence of MnO_2 and MnSe. The potential advantages which can be obtained from a MnO_2/MnSe heterostructure are: (1) As a result of the molecular-scale thickness of the materials, nearly all of the active sites are located on the surface; (2) the direct contact between MnO_2 and MnSe makes it simpler for ions and electrons to move across the surface of the active material; and (3) the MnO_2/MnSe heterostructure channels are well suited for the efficient transport of ions.

Herein, we demonstrated a novel heterostructured MnO_2/MnSe-NR@CC with a high aspect ratio by a straightforward and facile hydrothermal process. Experiments have demonstrated that adding selenium atoms to oxygen sites reduces electronegativity, increasing the intrinsic electronic conductivity of MnO_2 and decreasing electrostatic interactions with electrolyte ions, which boosts the reaction kinetics. As expected, novel heterostructured MnO_2/MnSe-NR@CC as an electrode for SC exhibits a high capacitance of 740.63 F/g at a current density of 1.5 A/g, with excellent cycling performance (93% capacitance retention

after 500 cycles). To examine the practical applications of MnO_2/MnSe-NR@CC-ASC as a positive electrode, MnO_2/MnSe-NR@CC//AC device was fabricated. The MnO_2/MnSe-NR@CC//AC-ASC device performed exceptionally well, with a maximum capacitance of 166.66 F/g at 2 A/g, with a capacitance retention of 94%, after 5000 GCD cycles. Additionally, it delivers an energy density of 75.06 Wh/kg at a power density of 1805.1 W/kg, and maintains 55.044 Wh/kg at a maximum power density of 18,159 W/kg. This research sheds fresh information on the anionic doping method and has the potential to be applied to the synthesis of positive electrode materials for energy storage applications.

2. Experimental method

2.1. Synthesis of MnO_2-NR@CC

The MnO_2-NR@CC precursor was prepared via a straightforward and facile hydrothermal process, where CC was employed as a template, and MnO_2-NRs were grown on the CC surface. First, 4 mg of potassium permanganate ($KMnO_4$) was dissolved in 40 mL of distilled water and stirred for 1 h, and a purple solution was obtained. Afterward, the dried CC supporting substrate was placed with the side wall of the Teflon-lined stainless steel autoclave and a glass slide was used to cover up one side of the CC to prevent growth on both sides of the CC substrate. Only the backside of the CC substrates were coated with the glass slide. Considering the CC substrate was only 0.2 mm thick, we were unable to cover the top and bottom with a glass slide. The above purple solution was transferred into a 100 mL Teflon-lined stainless steel autoclave and left for hydrothermal process in an oven at 180 °C for 6 h. After cooling down to room temperature, the resultant residue was cleaned repeatedly with distilled water and dried for 12 h at 60 °C.

2.2. Synthesis of heterostructured MnO_2/MnSe-NR@CC

To fabricate heterostructured MnO_2/MnSe-NR@CC, Se was loaded onto MnO_2-NR in a tube furnace with an argon environment. First, we loaded a porcelain boat with Se powder (99.9% Sinopharm), carefully positioned it upstream of the furnace, and then loaded a second porcelain boat with MnO_2-NR and positioned it downstream of the furnace and maintained a 350 °C furnace temperature. In the end, the samples were heated for 2 h at a ramping rate of 5 °C/min, and heterostructured MnO_2/MnSe-NR@CC was obtained.

2.3. Physical characterization

The morphology and structures of the fabricated sample were analyzed using a field emission scanning electron microscope (FESEM, HITACHI SU8220) and a transmission electron microscope (TEM JEM-2100 F, JEOL). The crystal structure of the sample was analyzed using X-ray diffraction (XRD, X'Pert Pro PANalytical) with Cu K (= 0.15406 nm) radiation. To investigate the elemental composition and valence state, X-ray photoelectron spectroscopy (XPS) technique was implemented.

2.4. Assembly of single electrode and SC device

The electrochemical measurements were performed in two and three-electrode setups. For three-electrode setup, the heterostructured MnO_2/MnSe-NR@CC with an active area of 1 × 1 cm^2 was directly used as a working electrode. The mass loading of the active substance on the CC was about 1.3 mg/cm^2. Ag/AgCl was used as a reference electrode and platinum wire as a counter electrode in 1 M sodium sulphate (Na_2SO_4) electrolyte. To assemble an asymmetric supercapacitor (ASC), the heterostructured MnO_2/MnSe-NR@CC membrane was employed as the positive electrode and activated carbon (AC) as the negative electrode (denoted as MnO_2/MnSe-NR@CC//AC-ASC) in an aqueous 1 M Na_2SO_4 solution. With the help of a microbalance, the mass loading density of the positive and negative electrode materials was carefully measured in the range of 1–1.3 mg/cm^2.

2.5. Electrochemical performance

An electrochemical workstation (CHI 660 E, China) was used to perform cyclic voltammogram (CV), galvanostatic charge-discharge (GCD) tests, and electrochemical impedance spectroscopy (EIS) measurements. The CV investigations were performed in a potential window range of 0.0–0.8 V; GCD investigations were performed at varying current densities range of 1.5–50 A/g, and EIS measurements were carried out at a frequency range of 0.001–100 kHz.

2.6. Calculations

The specific capacitance C_{sp} (F/g), the energy density E (Wh/kg), the power density P (W/kg), and the Coulombic efficiency (η) of the SC device can be calculated according to the following equations;

$$C_{sp} = \frac{I\Delta t}{m \times \Delta V} \tag{1}$$

$$C_d = \frac{I\Delta t_d}{M \times (V)} \tag{2}$$

$$E = 0.139 \times C_d V^2 \tag{3}$$

$$P = \frac{E}{\Delta t} \tag{4}$$

where I (A) is the current, Δt (s) is the discharge time, m (g) is the mass of the positive electrode, M (g) is the mass of the device, and ΔV(V) is the potential window.

3. Results and discussion

Fig. 1 illustrates a schematic diagram for the synthesis process of a novel nano-rod (NR)-shaped heterostructured manganese dioxide/manganese selenide (MnO_2/MnSe) on carbon cloth (CC) (denoted as MnO_2/MnSe-NR@CC). The MnO_2-NR was promptly grown at CC by a straightforward and facile hydrothermal process. MnSe was then loaded onto MnO_2-NR and annealed at 350 °C for 2 h in argon (Ar); thus, crystalline and mechanically stable heterostructured MnO_2/MnSe-NR@CC was obtained. An enlarged view of the Na^+ and SO^{4-} ions flow in the heterostructured MnO_2/MnSe-NR@CC from the Na_2SO_4 electrolyte can be seen in the upper part of the schematic diagram.

The morphology and structure of heterostructured MnO_2/MnSe-NR@CC were examined using a field emission scanning electron microscope (FESEM) and transmission electron microscope (TEM). FESEM images presented an in-depth overview of the heterostructured MnO_2/MnSe-NR@CC, composed of one-dimensional (1D) nanorods, as illustrated in Fig. 2a and b. The MnO_2/MnSe-NR@CC extends to a few micrometres in length. Each nanorod possessed a flaky appearance, and the construction of incredibly thin nanosheets into a web of interlinked pores offered a sizable and open active area. A medium-resolution FESEM image of the MnO_2/MnSe-NR@CC is shown in Fig. 2c, revealing nano-rod-like structures and uniform distribution of abundant cavities over the CC. Fig. 2d shows the high-resolution FESEM image, exhibiting well-retained nanorod-like structures with MnSe nanoparticles onto the MnO_2-NR@CC, thus forming open and porous structures by extensive interconnection. Additionally, TEM and high-resolution TEM (HRTEM) were used to examine the sample's structure and morphology. Fig. 2e shows the TEM image of heterostructure MnO_2/MnSe-NR@CC, which confirms that the as-prepared MnO_2 possesses nano-rod-shaped structures with densely distributed MnSe nanoparticles over the MnO_2-NR@CC, consistent with the aforementioned FESEM findings. According to the HRTEM image, Se doping introduces an amorphous surface with widespread defects and an interface

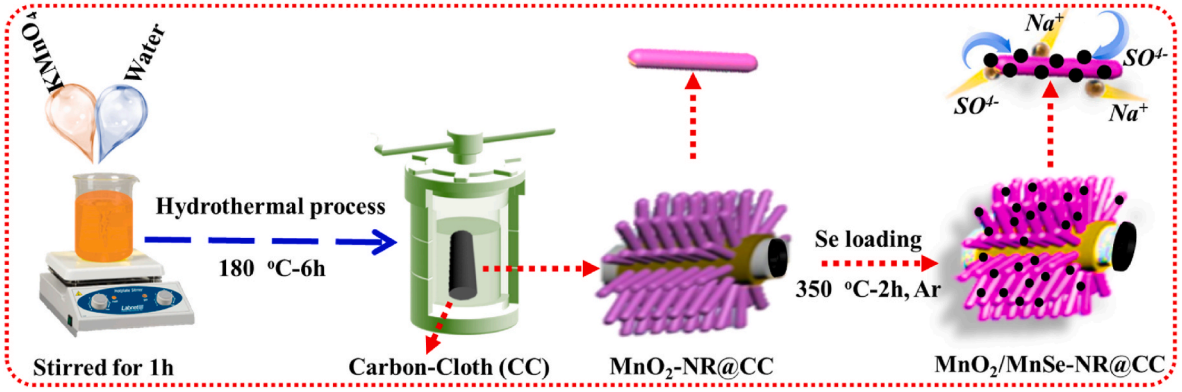

Fig. 1. Schematic diagram of the synthesis process of heterostructured MnO_2/MnSe-NR@CC by a facile hydrothermal method.

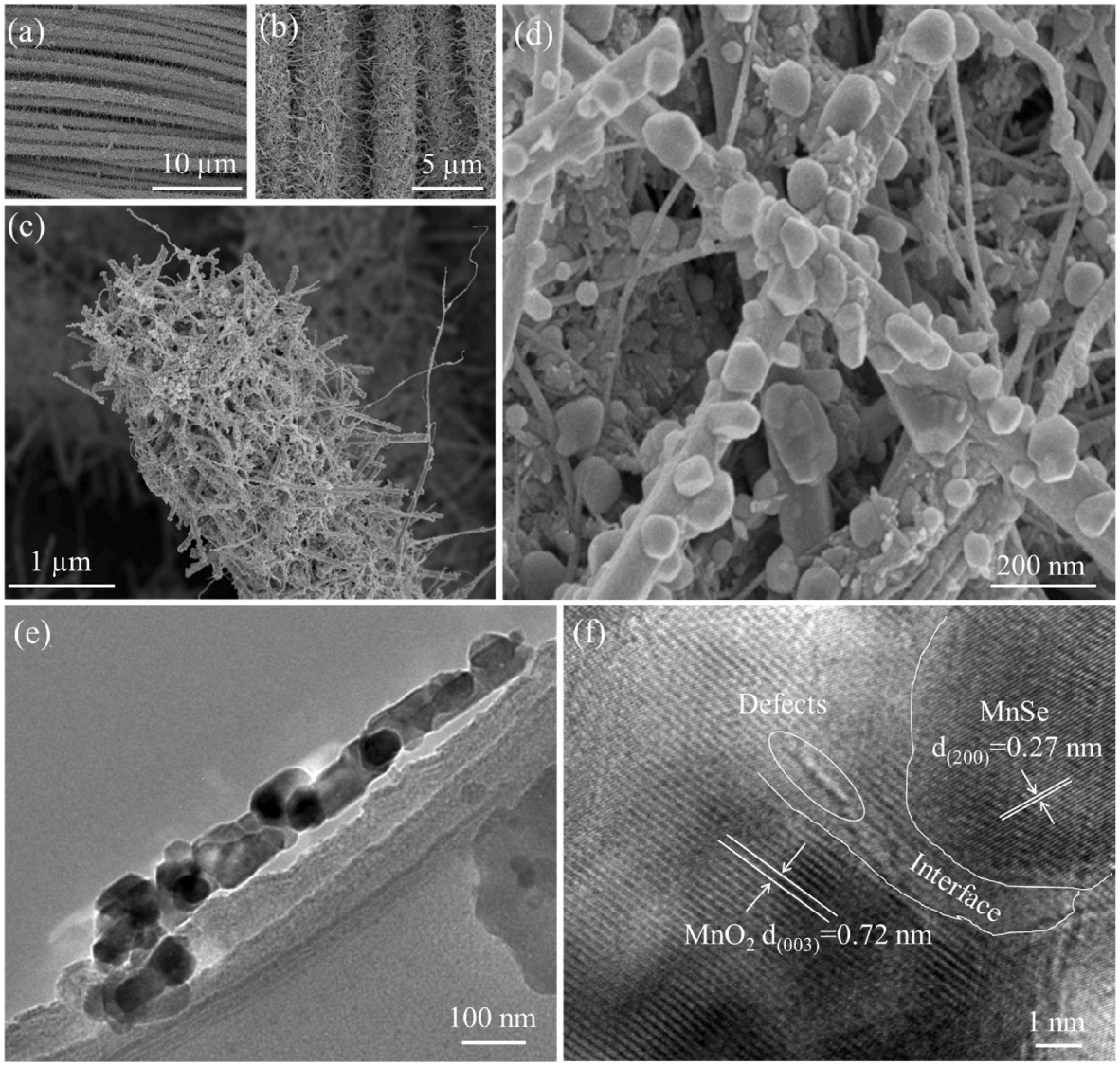

Fig. 2. FESEM images of heterostructured MnO_2/MnSe-NR@CC (a–c) Low-resolution, (d) High-resolution, TEM images of heterostructured MnO_2/MnSe-NR@CC (e) Low-resolution, (f) High-resolution TEM image.

of MnO_2 and MnSe, as shown in Fig. 2f, contributing to the formation of additional charge storage sites with pseudocapacitive properties. Moreover, the average value of the interplanar spacing of 0.72 nm and 0.27 nm corresponds to (003) planes of MnO_2 and (200) planes of MnSe, respectively.

Using X-ray powder diffraction (XRD), the as-prepared MnO_2-NR and MnO_2/MnSe-NR materials were investigated. Fig. 3a shows the XRD patterns of MnO_2 and heterostructure MnO_2/MnSe-NR. The XRD pattern

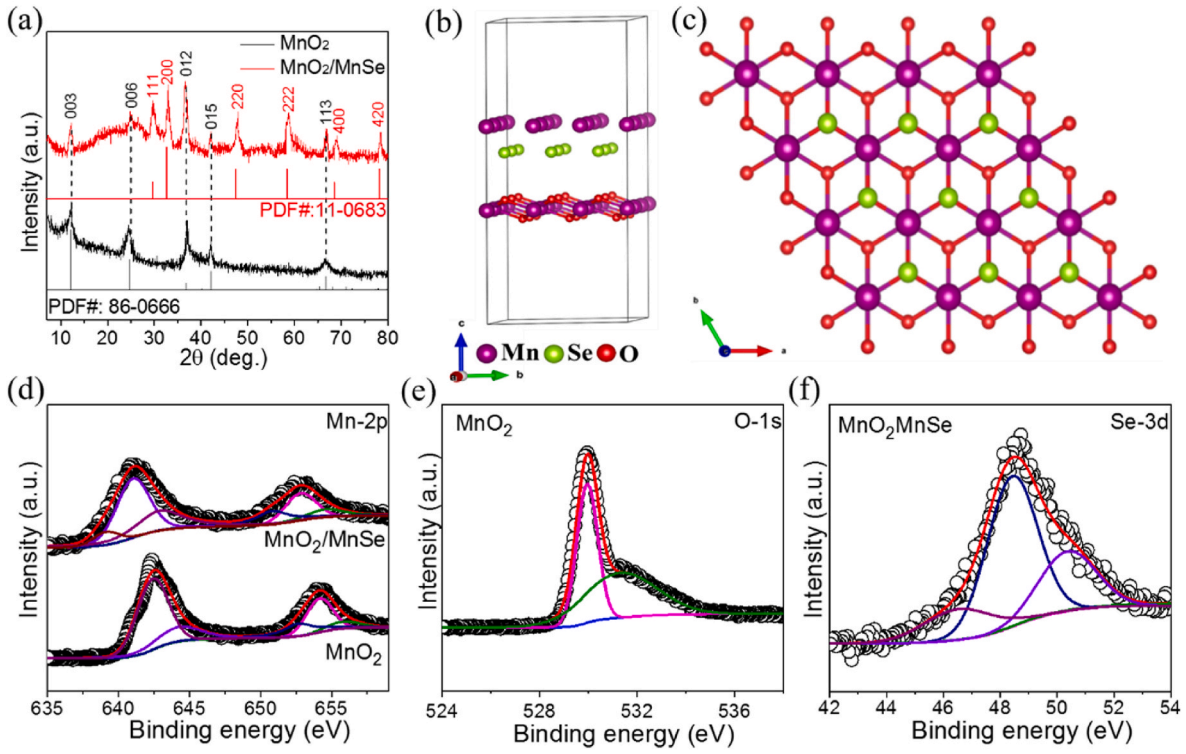

Fig. 3. (a) XRD patterns of MnO_2 and heterostructured MnO_2/MnSe-NR@CC, (b, c) Schematic diagrams of crystal structure of heterostructured MnO_2/MnSe-NR@CC, High-resolution XPS spectra of (d) Mn-2p, (e) O-1s, (f) Se-3d.

of MnO_2-NR shows the well-defined characteristic peaks were observed at 12.28°, 24.69°, 36.78°, 42.13°, and 66.80°, which correspond to the (003), (006), (012), (015), and (113) planes of δ-MnO_2 phase (JCPDS: 86–0666) (Zhao et al., 2017). On the other hand, the XRD pattern of MnO_2/MnSe-NR exhibits the new characteristic peaks were observed at 2θ values of 29.63°, 32.70°, 47.47°, 58.47°, 68.63°, and 78.20° and according to JCPDS: 11–0683, associated with the (111), (200), (220), (222), (400) and (420) planes of cubic α-MnSe (Miao et al., 2021). Compared to MnO_2, the peak intensity of (003) crystal planes for MnO_2/MnSe is faintly diminished. Moreover, there is no extra impurity diffraction peak, indicating that pure MnO_2 and MnSe have been effectively synthesized. Normally, in the MnO_2 crystal structure, the organization of basic MnO_6 octahedron units with varied connectivity results in the formation of polymorphs. These arrangements can either produce layer structures or chain/tunnel structures. MnO_6 octahedra can connect to other MnO_6 octahedra in a way that forms [MnO_6] chains in a direction parallel to the c-axis and creates tunnels between this chains (Baral et al., 2021). Here, after doping the Se atoms, the resulting crystal structure of heterostructure MnO_2/MnSe is illustrated in Fig. 3b and c, which depicts the corresponding comparable atomic structural models of MnO_2/MnSe. This model features a MnO_2 crystal phase, and the oxygen atoms in MnO_2 have been replaced with selenium atoms, suggesting the successful doping of Se in MnO_2 crystal.

The surface chemistry and valence state of MnO_2 and MnO_2/MnSe was further evaluated using X-ray photoelectron spectroscopy (XPS). Fig. 3d illustrates the high-resolution Mn-2p spectra for MnO_2 and MnO_2/MnSe. All of the spectra can be deconvoluted into two peaks which correspond to Mn-$2p_{3/2}$ (642.5 eV) and Mn-$2p_{1/2}$, (654.2 eV) of MnO_2, while Mn-$2p_{3/2}$ (641.1 eV) and Mn-$2p_{1/2}$, (652.8 eV) of MnO_2/MnSe. Further, the spin energy difference remains constant at 11.7 eV for both the MnO_2 and MnO_2/MnSe samples. Compared to MnO_2, the Mn-2p peaks of MnO_2/MnSe shifted towards lower binding energy. Furthermore, the insertion of oxygen defects increased the signal of Mn^{3+} while decreasing the signal of Mn^{4+} significantly (Wang et al., 2020b; He et al., 2018). The high-resolution O-1s spectra were fitted into two peaks with binding energies at 529.9 eV and 531.4 eV, which could be ascribed to the tetravalent Mn–O–Mn bond and oxygen defect, respectively, as shown in Fig. 3e (Zeng et al., 2018). Fig. 3f exhibits the high-resolution Se-3d spectra of the MnO_2/MnSe sample. The Se-3d spectrum can be deconvoluted into three peaks. The peak located at a binding energy of 54.47 eV can be associated with the Se-$3d_{5/2}$, and the peak positioned at a binding energy of 55.50 eV can be attributed to $Se3d_{3/2}$, confirming the existence of Se^{2-} ions in the sample and the third peak at 57.6 eV can be related to Se–O (Xing et al., 2021).

The MnO_2 and MnO_2/MnSe-NR@CC were studied as positive electrodes for SC, and the electrochemical measurements were tested in 1 M Na_2SO_4 aqueous electrolyte in a three-electrode setup. The cyclic voltammogram (CV) profiles of MnO_2 and heterostructured MnO_2/MnSe-NR@CC electrodes within a potential window range of 0–0.8 V and at a scan rate 10 mV/s are shown in Fig. 4a. To examine the contribution of MnO_2 to total capacitance, CV measurements of pure MnO_2 without Se were performed. CV profiles of the MnO_2 electrode show that the contribution of pure MnO_2 without Se was insignificant. Compared to the MnO_2 electrode, the heterostructured MnO_2/MnSe-NR@CC electrode's CVs are more rectangular with a pair of redox peaks, indicating superior capacitive behaviour. As seen in the following equation (5), the redox reactions are;

$$MnO_2 + Na^+ + e^- \rightleftharpoons MnO_2^-Na^+ \quad (5)$$

The adsorption of the proton (alkali metal cations (Na^+)) to the surface of active material, or desorption from the surface of the active material, provides the basis for the process, as shown in Equation (5). This involves a surface redox process that is reversible and occurs between Mn^{4+} and Mn^{3+} ions (Weng et al., 2015). Further, the area under CV profiles is larger, suggesting a high specific capacitance heterostructured MnO_2/MnSe-NR@CC electrode. Obtaining a greater current at the heterostructured MnO_2/MnSe-NR@CC electrode than at the MnO_2 electrode suggests improved electron transport and Se consumption. These better capabilities of the Se-doped MnO_2-NR can be attributed to the high contact area between the active material, and the

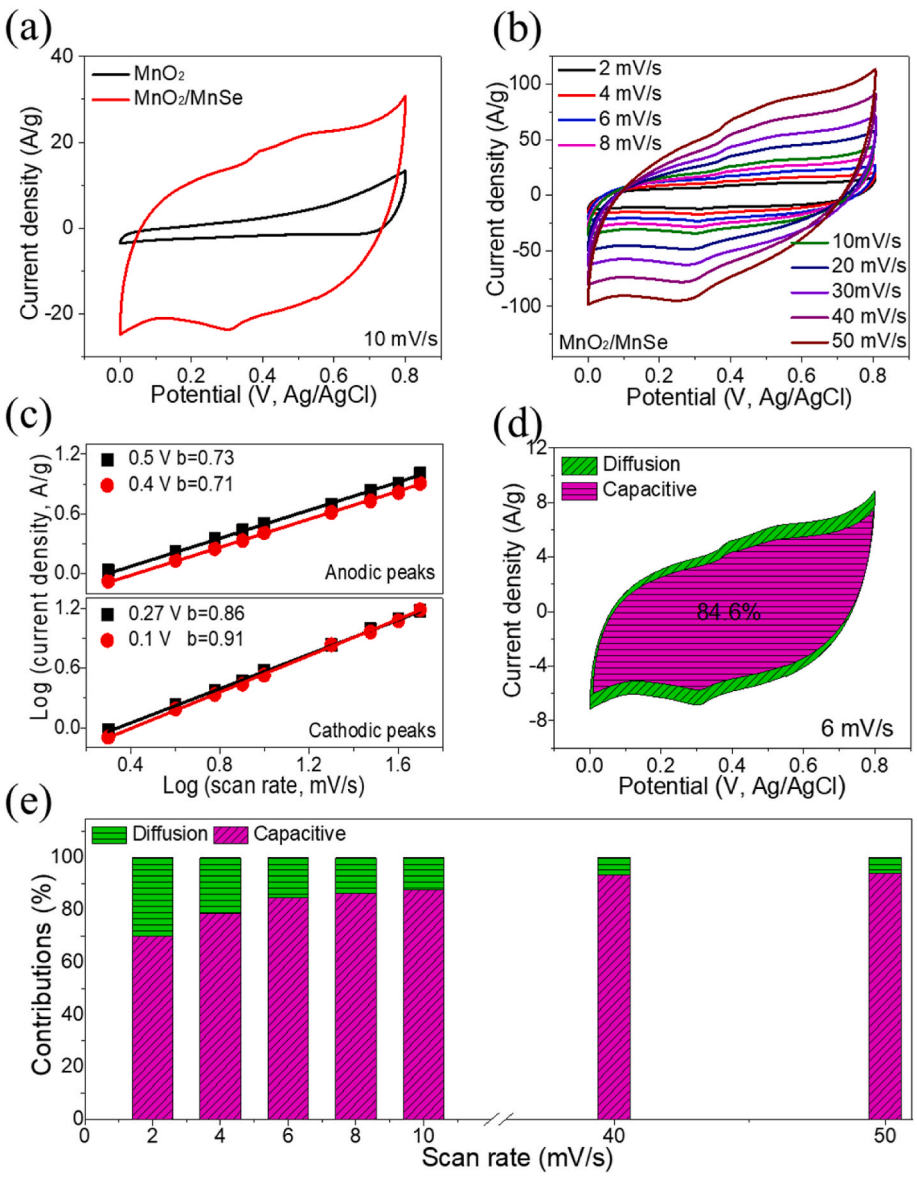

Fig. 4. (a) CV profiles of MnO_2 and heterostructured MnO_2/MnSe-NR@CC electrodes in 1 M Na_2SO_4 aqueous electrolyte at 10 mV/s, (b) CV profiles of heterostructured MnO_2/MnSe-NR@CC electrode at various scan rates from 2 to 8 mV/s), (c) Calculation of *b*-values log (*i*) versus log (*v*), (d) Diffusion- and capacitive-controlled contribution from the total stored charge at 6 mV/s, (e) Contribution ratio between capacitive- and diffusion-controlled charge storage at various scan rates from 2 to 50 mV/s.

current collector can greatly reduce the length of the electron transport channel. This promotes quick ions diffusion during the charging and discharging operation. CV measurements of the heterostructured MnO_2/MnSe-NR@CC electrode were also performed at various scan rates, and the results are shown in Fig. 4b. The outstanding capacitive performance of the heterostructured MnO_2/MnSe-NR@CC electrode is shown by the presence of a rectangular consistency with a pair of redox peaks in each of these curves when measured at a variety of scan rates ranging from 10 to 50 mV/s. In addition, the charge storage process of heterostructured MnO_2/MnSe-NR@CC electrode was investigated by the analysis of the electrochemical kinetics according to power law (Mateen et al., 2022; Javed et al., 2021b);

$$i(V) = a.v^b \tag{6}$$

$$\log(i) = \mathrm{b}\,\log(v) + \log(a) \tag{7}$$

where *i* represents the peak current density, *v* represents the scan rate, and *a* and *b* represent arbitrary constants. It is important to note that if it approaches 1.0, the capacitive process will dominate and if the b-value approaches 0.5, the diffusion-controlled process dominates (Chodankar et al., 2020). According to equation (7), which is the relation between log *i* and log (*v*), the anodic b-values for heterostructured MnO_2/MnSe-NR@CC electrode are 0.73, 0.71 (at potential 0.5 and 0.4 V) while the cathodic b-values are 0.86, 0.91 (at potential 0.27 and 0.1 V) as exhibited in Fig. 4c. It suggests that both diffusion-controlled and capacitive-controlled processes contribute to total charge storage. Further, the quantitatively diffusion-controlled and capacitive-controlled contributions of heterostructured MnO_2/MnSe-NR@CC electrode were calculated according to the following equation (8).

$$i(V) = k_1 v + k_1 v^{1/2} \tag{8}$$

where *i* denotes the total current, the terms k_1v and $k_1v^{1/2}$ show the capacitive-controlled and diffusion-controlled charge storage process, respectively, k_1 and k_2 represents arbitrary constants. At a scan rate of 6 mV/s, the capacitive-controlled process is dominant. It was found that 84.6% of the total charge is stored through the capacitive-controlled process, while 15.6% is stored through the diffusion-controlled process for heterostructured MnO_2/MnSe-NR@CC electrode, as illustrated in Fig. 4d. Fig. 4e exhibits the capacitive-controlled and diffusion-controlled contributions from total charge storage at different scan rates ranging from 2 to 50 mV/s for heterostructured MnO_2/MnSe-

NR@CC electrode. It was found that the capacitive-controlled process for charge storage exhibits the highest percentage of total charge storage for heterostructured MnO_2/MnSe-NR@CC electrode.

To find out more about the ability of MnO_2 and heterostructured MnO_2/MnSe-NR@CC electrodes to store charge, galvanostatic charge/discharge (GCD) studies were performed. The comparative GCD profiles of MnO_2 and heterostructured MnO_2/MnSe-NR@CC electrodes in the potential window range of 0.0–0.8 V and at a current density of 5 A/g are exhibited in Fig. 5a. The heterostructured MnO_2/MnSe-NR@CC electrode has a longer discharge duration than the MnO_2 electrode, which is consistent with the CV measurements. Further, the comparative GCD profiles of heterostructured MnO_2/MnSe-NR@CC electrode at various scan rates from 1.5 to 50 A/g are illustrated in Fig. 5b. The symmetrical GCD profiles represent pseudocapacitive charge storage. Further, an initial reversal drop (IR-drop) is a possible drop seen at the start of the discharge curve. The intrinsic resistance of the electrode material and the resistance of the electrolyte are quantified by the IR drop. The former often contributes more to the total IR drop, as illustrated in Fig. 5b. The observed IR-drop for the MnO_2/MnSe-NR@CC electrode is about 0.03 and 0.08 V, respectively, for current densities ranging from 1.5 to 50 A/g. The extremely low iR-drop can be attributed to the exceptionally high ion conductivity of electrode and electrolyte, and according to the literature, the potential drop rises almost linearly with current density (Javed et al., 2018; Khan et al., 2019). At different current densities from 1.5 to 50 A/g, the specific capacitance of MnO_2 and heterostructured MnO_2/MnSe-NR@CC electrodes were also calculated using equation (1), and the results are displayed in Fig. 5c. The highest specific capacitance of heterostructured MnO_2/MnSe-NR@CC electrodes was calculated and followed as 740.63, 693.75, 646.88, 630, 592.50, 562.50 and 531.25 F/g at 1.5, 3, 5, 8, 12, 25, and 50 A/g, respectively. However, the maximum specific capacitance of the MnO_2 electrode was computed as 264.51, 247.76, 235.03, 212, 201.61, 174.89, and 149.73 F/g at 1.5, 3, 5, 8, 12, 25, and 50 A/g, respectively. The impressive rate capability of 71.7% at 50 A/g from the heterostructured MnO_2/MnSe-NR@CC electrode, which is more than that of the MnO_2 electrode (56.7% at 50 A/g), making it a suitable option for use in the development of future generation supercapacitor. To get a better electrochemical performance and the redox kinetics of the heterostructured MnO_2/MnSe-NR@CC electrode, electrochemical impedance spectroscopy (EIS) measurements were performed at open circuit potential. The Nyquist plot of the heterostructured MnO_2/MnSe-NR@CC electrode is illustrated in Fig. 5d. The Nyquist plot comprises three

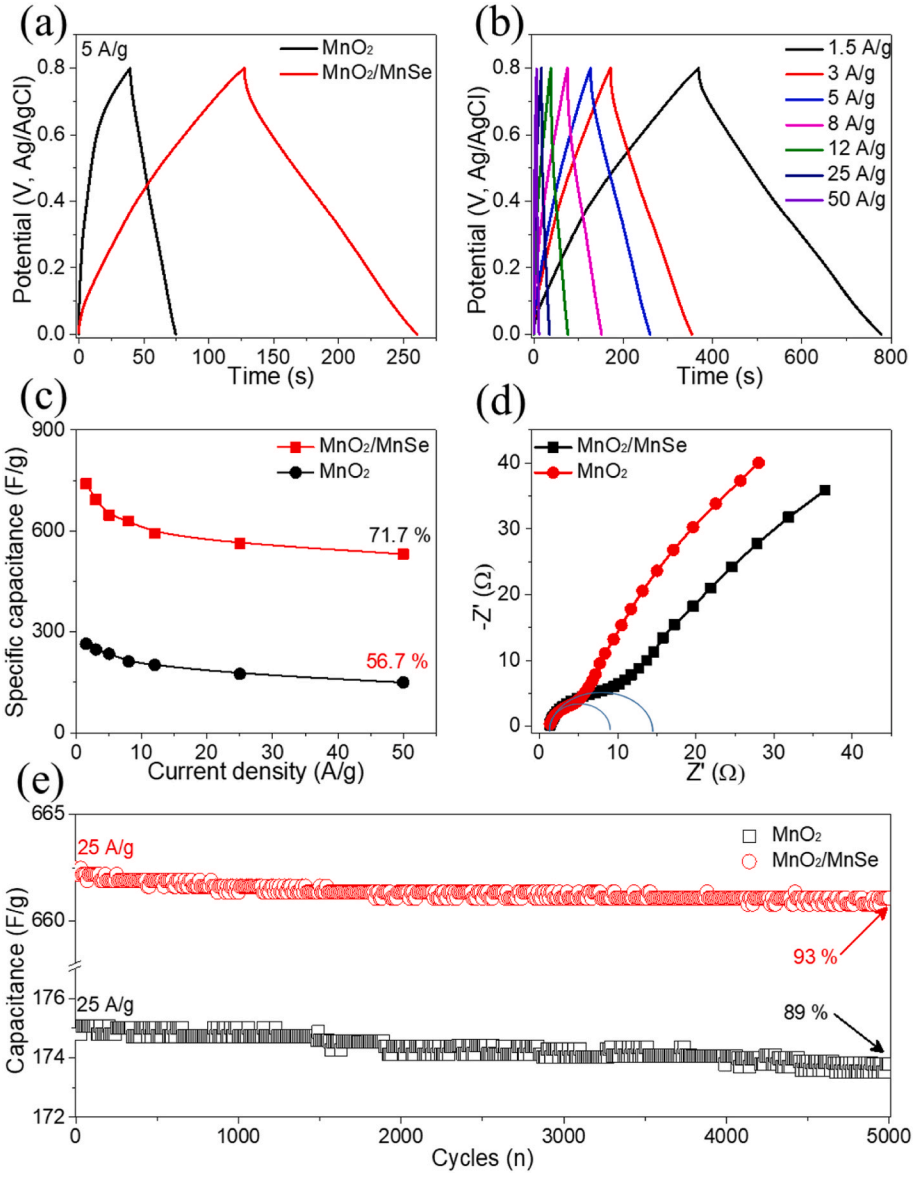

Fig. 5. (a) GCD profiles of MnO_2 and heterostructured MnO_2/MnSe-NR@CC electrodes at 5 A/g, (b) GCD profiles of heterostructured MnO_2/MnSe-NR@CC electrode at various current densities from 1.5 to 50 A/g, (c) specific capacitance of MnO_2 and heterostructured MnO_2/MnSe-NR@CC electrodes at various current densities from 1.5 to 50 A/g, (d) Nyquist plot of MnO_2 and heterostructured MnO_2/MnSe-NR@CC electrodes, (e) Cycling performance of MnO_2 and heterostructured MnO_2/MnSe-NR@CC electrodes.

segments: a semicircle in the high-frequency section, an intercept with the x-axis, and a quasi-vertical straight line in the low-frequency section. The x-intercept yields the equivalent series resistance (R_s), which consists of the inherent resistance of the electrode and electrolytic resistance. The diameter of the semicircle is related to charge transfer resistance (R_{ct}), while the slope of the vertical line is related to the Warburg element and is known as electrolytic ion diffusion resistance. At the high-frequency section, the values of R_{ct} from the diameter of a semicircle for the heterostructured MnO_2/MnSe-NR@CC electrode was 7.83 Ω, and for the MnO_2 electrode was 13.37 Ω. The values of R_s from the intercept of the real axis for heterostructured MnO_2/MnSe-NR@CC and MnO_2 electrodes were computed to be 1.34 and 1.41, respectively. This indicates that the heterostructured MnO_2/MnSe-NR@CC electrode has high electrical conductivity. Based on the above studies, the heterostructured MnO_2/MnSe-NR@CC electrode has outstanding electrochemical properties. Because the cycling stability of SCs for commercial applications is likewise of the utmost importance, extended cycles are performed for heterostructured MnO_2/MnSe-NR@CC and MnO_2 electrodes at a high current density of 25 A/g. Fig. 5e demonstrates that after 5000 GCD cycles, heterostructured MnO_2/MnSe-NR@CC electrodes maintain capacitance retention of 93%, whereas MnO_2 electrodes retain only 89% of their original capacitance. It confirms the outstanding energy-storage capability of the heterostructured MnO_2/MnSe-NR@CC electrode throughout the repeated charge-discharge cycle. Additionally, the electrochemical performance of MnO_2/MnSe-NR@CC, compared to other MnO_2-based nanostructured electrode materials for SCs, is summarized in Table 1. The comparison reveals that the electrochemical performance of the MnO_2/MnSe-NR@CC electrode material is superior to that of previously studied related materials.

To explore the potential practical applications of heterostructured MnO_2/MnSe-NR@CC as a positive electrode, an asymmetric SC device (MnO_2/MnSe-NR@CC//AC-ASC) was assembled using activated carbon (AC) as a negative electrode and 1 M Na_2SO_4 aqueous electrolyte. The asymmetric SC arrangement is preferred because it has a larger working potential window and a greater energy density. Fig. 6a displays the results of a CV analysis performed at a constant scan rate of 10 mV/s on MnO_2/MnSe-NR@CC and AC electrodes in their respective potential windows. The CV demonstrates the features of a pseudocapacitor for the MnO_2/MnSe-NR@CC electrode, whereas the AC electrode exhibited the characteristics of an electric double layer in the potential window range of 0.0–0.8 V and −1.0-0.0 and 0.0–0.8 V respectively. The mass balance of the assembled positive and negative electrodes was calculated according to the following equation (Karuppaiah et al., 2020);

$$\frac{m^+}{m^-} = \frac{(C^- \times \Delta V^-)}{(C^- \times \Delta V^+)} \tag{9}$$

Where ΔV^+ and ΔV^- represent the potential difference between the positive and negative electrodes, C^+ and C^- represent the specific capacitance of the positive and negative electrodes, and m^+ and m^- represent the masses of the positive and negative electrodes. To identify the maximum stable operating potential window of the MnO_2//MnSe-NR@CC//AC-ASC, multiple CV measurements were performed at varying potential windows at a scan rate of 10 mV/s, as shown in Fig. 6b. At a potential of 2 V, a sharp increase in anodic current was seen along the CV profile, which indicates oxidation. It was concluded that a potential window ranging from 0.0 to 1.8 V would be ideal for preventing the generation of gases, and this optimal potential window was employed for all further measurements. As seen in Fig. 6c, the CV profiles of MnO_2/MnSe-NR@CC/AC-ASC were obtained at various scan rates ranging from 2 to 60 mV/s in a potential window of 0–1.8 V. Even at higher scan rates, the CV profiles retained their shapes with very small modifications, and the area under CV profiles gradually increased with scan rates. It indicates that MnO_2/MnSe-NR@CC/AC-ASCC demonstrates an excellent pseudocapacitive behavior and good charge/discharge capacity, and the device possesses excellent electrochemical performance. Further, the GCD measurements were carried out at various current densities from 2 to 20 A/g in a potential window of 0–1.8 V, as illustrated in Fig. 6d. The symmetrical GCD profiles indicate pseudocapacitive charge storage characteristics of MnO_2/MnSe-NR@CC//AC-ASC. The maximum specific capacitance (C_d) of the MnO_2/MnSe-NR@CC//AC-ASC device can be calculated using equation (2), by the total mass of active material on both positive and negative electrodes and discharging time. The calculated specific capacitance values are 166.6, 150, 138.8, 132.2, 127.7, and 122.2 F/g, at current densities of 2, 3, 5, 7, 10, and 20 A/g, and specific capacitance is plotted as a function of current density, as illustrated in Fig. 6e. As the current density was increased from 2 to 20 A/g, 73% of the capacitance retention was obtained, which indicates an outstanding rate performance of the MnO_2/MnSe-NR@CC//AC-ASC device. To investigate the practical strength of the MnO_2/MnSe-NR@CC//AC-ASC device, the energy density (E) and power density (P) were calculated using equations (3) and (4), respectively, via the total mass of both positive and negative electrodes.

The Ragone plot, which demonstrates the E and P of the MnO_2/MnSe-NR@CC//AC-ASC device, is shown in Fig. 6f. The MnO_2/MnSe-NR@CC//AC-ASC device delivers energy densities of 75.06, 67.554, 62.55, 59.5476, 57.546 and 55.044 Wh/kg at power densities of 1805.1, 2735.3, 4543.5, 6399.7, 8919.31 and 18,159 W/kg. In addition, the present MnO_2/MnSe-NR@CC//AC-ASC device is better as compared to many other previously investigated bimetallic oxide-based asymmetric SCs devices such as $CuGa_2O_4$//AC (38 Wh/kg, 286 W/kg) (Ji et al., 2020), $CoGa_2O_4$//AC (25.3 Wh/kg, 788 W/kg) (Cao et al., 2020), $NiCo_2O_4$//AC (60 Wh/kg, 750 W/kg) (Zhang et al., 2020b), Co_3O_4@CNT (72 Wh/kg, 533 W/kg)) (Xiao et al., 2017), $CoGa_2O_4$//AC (68 Wh/kg, 825 W/kg) (Zhu et al., 2019), $CoGa_2O_4$//$ZnFe_2O_4$ (37 Wh/kg, 414 W/kg) (Ji et al., 2019), $ZnCo_2O_4$//AC (30.5 Wh/kg, 750 W/kg) (Kumar et al., 2020), Co@Co_2O_4//AC (38 Wh/kg, 850 W/kg) (Qiu et al., 2020), and Zn–Ni–Al–Co//AC (35.6 Wh/kg, 700 W/kg) (Zhang et al., 2016b). The cyclic stability of the MnO_2/MnSe-NR@CC//AC-ASC device is exhibited in Fig. 6g, which shows capacitance retention of 94% after 5000 GCD cycles, suggesting an outstanding cycling performance. The results of the three- and two-electrode systems reveal that the

Table 1
A comparison of MnO_2-based supercapacitor electrodes reported in previously published works.

Sr. No	Electrode material	Electrolyte	Specific capacitance (F/g)	Current density (A/g)	Capacitance retention (%)	No of Cycles (n)	Ref.
1.	α-MnO_2	Na_2SO_4	200	1	87.6	1000	Zhang et al. (2012)
2.	MnO_2@ NGO	KOH	360	0.5	90	6000	Ramesh et al. (2019)
3.	MnO_2-CNFs	Na_2SO_4	324.55	0.5	62	1000	Liu et al. (2021)
4.	MnO_2/PANI/GN	Na_2SO_4	472	1	79.7	5000	Wu et al. (2017)
5.	MnO_2/RGO	Na_2SO_4	347	1	93.1	2500	Zhang et al. (2020a)
6.	rGO/MnO_2	KOH	486.48	0.85	75.8	2000	Parveen et al. (2017)
7.	α-Fe_2O_3/MnO_2	KOH	216	1	89. 2	1000	Racik K et al. (2020)
8.	α-MnO_2 nanowires	Na_2SO_4	362	1	83	5000	Shah et al. (2018b)
9.	MnO_2/g-C_3N_4	Na_2SO_4	211	1	90	1000	Chang et al. (2017)
10.	MnO_2/$MnCo_2O_4$	KOH	497	0.5	60	5000	Zhang et al. (2016a)
11.	**MnO_2/MnSe-NR@CC**	**Na_2SO_4**	**740.63**	**1.5**	**93**	**5000**	**This work**

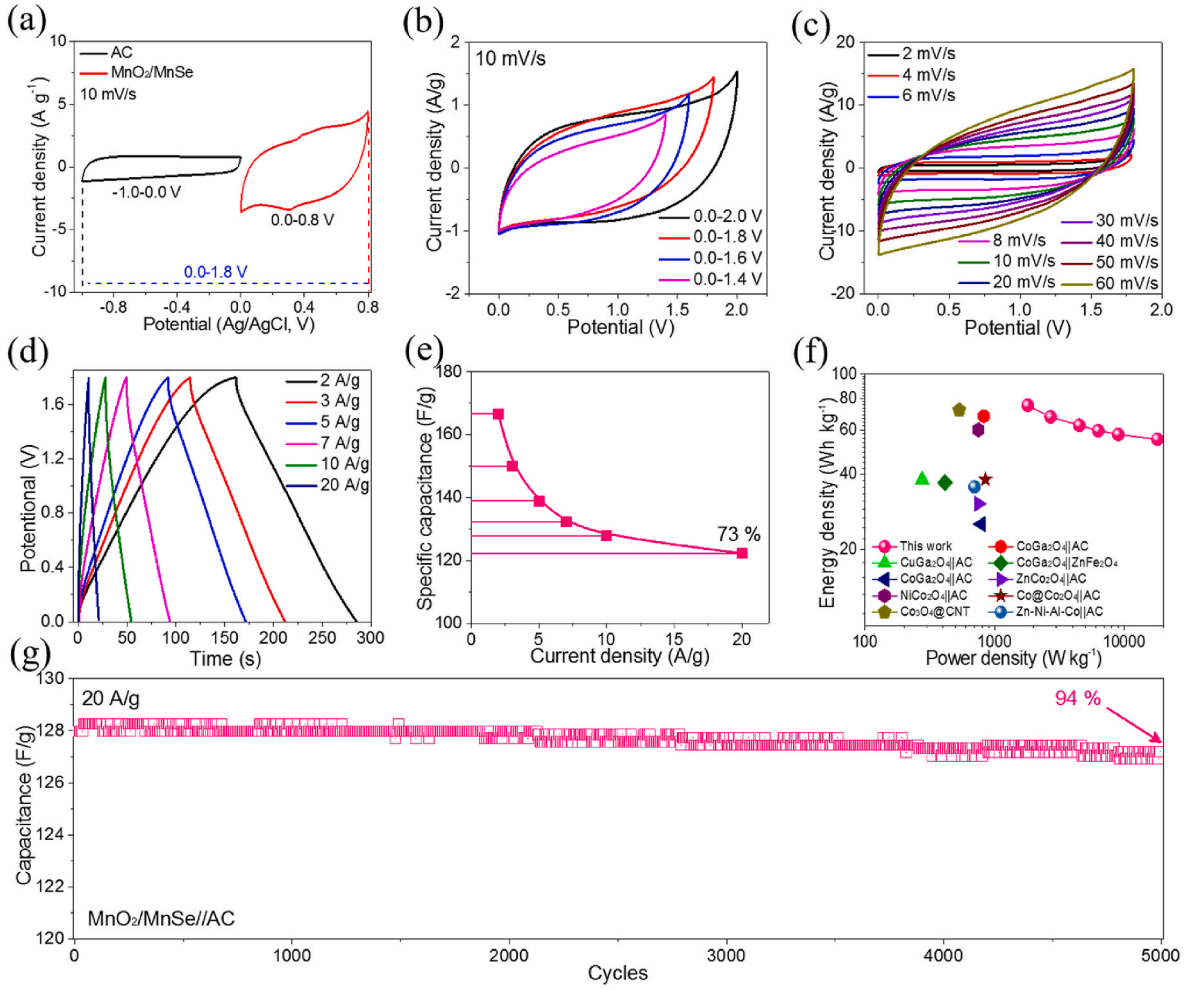

Fig. 6. Electrochemical characterization of MnO_2/MnSe-NR@CC//AC-ASC in a two-electrode setup: (a) CV profiles of both positive and negative electrodes at 10 mV/s, (b) CV profiles of MnO_2/MnSe-NR@CC//AC-ASC at 10 mV/s and in various potential window ranges, (c) CV profiles at various scan rates, (d) GCD profiles at various current densities, (e) Specific capacitance at various current densities from 2 to 20 A/g, (f) Ragone plot and comparison with previously reported results, (g) long-term cycling performance test.

MnO_2/MnSe-NR@CC electrode material displays a remarkable electrochemical performance, such as specific capacitance, cycling performance, energy density, and power density. We believe that the advantageous synergic composition and heterostructure of MnO_2/MnSe-NR@CC electrode material are responsible for these remarkable characteristics. Particularly, heterostructured MnO_2/MnSe-NR@CC offers a reasonably large active surface area and electrochemical activity when Se is present.

4. Conclusion

In summary, we demonstrated a novel heterostructured MnO_2/MnSe-NR@CC with a high aspect ratio by a straightforward and facile hydrothermal process. Experiments have demonstrated that doping selenium atoms to oxygen sites reduce electronegativity, increasing the intrinsic electronic conductivity of MnO_2, decreasing electrostatic interactions with electrolyte ions, and boosting the reaction kinetics. The heterostructured MnO_2/MnSe-NR@CC electrode shows an outstanding specific capacitance of 740.63 F/g at a current density of 1.5 A/g, with excellent cycling performance and maintained 93% capacitance retention after GCD 5000 cycles. Furthermore, the MnO_2/MnSe-NR@CC//AC-ASC device can operate in a wider potential window of 0.0–1.8 V. It delivers an ultrahigh energy density of 75.06 Wh/kg at a power density of 1805.1 W/kg, which is better than some other already reported bimetallic asymmetric SC devices. Additionally, the MnO_2/MnSe-NR@CC//AC-ASC delivers a maximum specific capacitance of 166.66 F/g at a current density of 2 A/g and retained 94% of its initial capacitance after 5000 cycles. The outstanding properties of this MnO_2/MnSe-NR@CC electrode material can be associated with synergic composition and nanostructure. Such excellent results proved that the Se loaded MnO_2–based electrode material is suitable for next-generation energy storage devices.

Author credit statement

Conception and design of study: Qasim Abbas, Muhammad Sufyan Javed, Abdul Mateen, Sajid Hussain Siyal. Acquisition of data: Qasim Abbas, Muhammad Sufyan Javed, Najam Ul Hassan, Asma A. Alothman, Mohamed Ouladsmane, Analysis and/or Interpretation of data: Muhammad Sufyan Javed, Mohd Zahid Ansari, Elsayed Tag Eldin, Najam Ul Hassan. Drafting the manuscript: Abdul Mateen, Najam Ul Hassan, Muhammad Sufyan Javed, Sajid Hussain Siyal, Elsayed Tag Eldin. Supervision: Muhammad Sufyan Javed, Mohd Zahid Ansari, Revising the manuscript critically for important intellectual content: Mohd Zahid Ansari, Elsayed Tag Eldin, Najam Ul Hassan, Abdul Mateen, Sajid Hussain Siyal, Qasim Abbas, Najam Ul Hassan, Asma A. Alothman, Mohamed Ouladsmane.

Declaration of competing interest

The authors declare that they have no known competing financial interests or personal relationships that could have appeared to influence the work reported in this paper.

Data availability

Data will be made available on request.

Acknowledgments

This work was financially supported by the Research Fund for International Scientists (52250410342), Scientific Research start-up grant for Youth Researchers at Lanzhou University and Supercomputing Center of Lanzhou University. This work was funded by the Researchers Supporting Project Number (RSP-2021/243) King Saud University, Riyadh, Saudi Arabia.

References

Arul, N.S., Han, J.I., 2016. Mater. Lett. 181, 345–349.
Azman, N.H.N., Sulaiman, Y., Mamat @ Mat Nazir, M.S., Lim, H.N., 2019. J. Mater. Sci. Mater. Electron. 30, 1458–1467.
Balamuralitharan, B., Karthick, S., Balasingam, S.K., Hemalatha, K., Selvam, S., Raj, J.A., Prabakar, K., Jun, Y., Kim, H.J.J.E.T., 2017. Energy Technol. 5, 1953–1962.
Baral, A., Satish, L., Zhang, G., Ju, S., Ghosh, M.K., 2021. J. Inorg. Organomet. Polym. Mater. 31, 899–922.
Cao, Z., Liu, C., Huang, Y., Gao, Y., Wang, Y., Li, Z., Yan, Y., Zhang, M., 2020. J. Power Sources 449, 227571.
Chang, X., Zhai, X., Sun, S., Gu, D., Dong, L., Yin, Y., Zhu, Y., 2017. Nanotechnology 28, 135705.
Chen, H., Chen, S., Fan, M., Li, C., Chen, D., Tian, G., K. J. J. o. M. C. A. Shu, 2015. J. Mater. Chem. 3, 23653–23659.
Chodankar, N.R., Pham, H.D., Nanjundan, A.K., Fernando, J.F., Jayaramulu, K., Golberg, D., Han, Y.K., Dubal, D.P.J.S., 2020. Small 16, 2002806.
Dinesh, M., Haldorai, Y., Rajendra Kumar, R.T., 2020. Ceram. Int. 46, 28006–28012.
Gao, Y.-P., Wu, X., Huang, K.-J., Xing, L.-L., Zhang, Y.-Y., Liu, L.J.C., 2017. CrystEngComm 19, 404–418.
Guo, W., Yu, C., Li, S., Wang, Z., Yu, J., Huang, H., Qiu, J., 2019. Nano Energy 57, 459–472.
He, H., Huang, D., Pang, W., Sun, D., Wang, Q., Tang, Y., Ji, X., Guo, Z., Wang, H.J. A.m., 2018. Adv. Mater. 30, 1801013.
Javed, M.S., Shah, H.U., Shaheen, N., Lin, R., Qiu, M., Xie, J., Li, J., Raza, R., Mai, W., Hu, C., 2018. Electrochim. Acta 282, 1–9.
Javed, M.S., Shah, S.S.A., Hussain, S., Tan, S., Mai, W., 2020. Chem. Eng. J. 382, 122814.
Javed, M.S., Khan, A.J., Hanif, M., Nazir, M.T., Hussain, S., Saleem, M., Raza, R., Yun, S., Liu, Z., 2021a. Int. J. Hydrogen Energy 46, 9976–9987.
Javed, M.S., Khan, A.J., Ahmad, A., Siyal, S.H., Akram, S., Zhao, G., Awadh Bahajjaj, A. A., Ouladsmane, M., Alfakeer, M., 2021b. Ceram. Int. 47, 30747–30755.
Javed, M.S., Mateen, A., Ali, S., Zhang, X., Hussain, I., Imran, M., Shah, S.S.A., Han, W.J. S., 2022. Small, 2201989.
Ji, P., Zhang, C., Wan, J., Zhou, M., Xi, Y., Guo, H., Hu, C., Gu, X., Wang, C., Xue, W., 2019. ACS Appl. Mater. Interfaces 11, 28900–28908.
Ji, Y., Deng, Y., Chen, F., Wang, Z., Lin, Y., Guan, Z., 2020. Carbon 156, 359–369.
Karuppaiah, M., Akilan, R., Sakthivel, P., Asaithambi, S., Shankar, R., Yuvakkumar, R., Hayakawa, Y., Ravi, G., 2020. J. Energy Storage 27, 101138.
Khan, A.J., Hanif, M., Javed, M.S., Hussain, S., Liu, Z., 2019. J. Mater. Sci. Mater. Electron. 30, 8568–8576.
Khan, A.J., Javed, M.S., Hanif, M., Abbas, Y., Liao, X., Ahmed, G., Saleem, M., Yun, S., Liu, Z., 2020. Ceram. Int. 46, 3124–3131.
Kumar, Y.A., Kumar, K.D., Kim, H.-J., 2020. Electrochim. Acta 330, 135261.
Liu, C.-S., Huang, C.-L., Fang, H.-C., Hung, K.-Y., Su, C.-A., Li, Y.-Y., 2021. J. Energy Storage 33, 102130.
Long, X., Tian, L., Wang, J., Zhang, L., Chen, Y., Emin, A., Wang, X., Xie, W., Liu, D., Fu, Y., Li, J., Li, Y., He, D., 2020. J. Electroanal. Chem. 877, 114656.
Majumdar, D.J.C., 2021. Chemelectrochem 8, 291–336.
Mateen, A., Javed, M.S., Khan, S., Saleem, A., Majeed, M.K., Khan, A.J., Tahir, M.F., Ahmad, M.A., Assiri, M.A., Peng, K.-Q., 2022. J. Energy Storage 49, 104150.
Miao, C., Fang, Y., Zhu, K., Zhou, C., Ye, K., Yan, J., Cao, D., Wang, G., Xu, P., Xie, C., 2021. J. Alloys Compd. 885, 161004.
Nagaraju, G., Cha, S.M., Sekhar, S.C., J. S. J. A. E. M. Yu, 2017. Adv. Energy Mater. 7, 1601362.
Parveen, N., Ansari, S.A., Ansari, M.O., Cho, M.H., 2017. J. Colloid Interface Sci. 506, 613–619.
Qiu, W., Xiao, H., H. J. J. o. P. S. Gao, 2021. J. Power Sources 491, 229583.
Qiu, H., Sun, X., Zhang, Y., He, W., 2020. Ceram. Int. 46, 8766–8773.
Racik K, M., Manikandan, A., Mahendiran, M., Madhavan, J., Victor Antony Raj, M., Mohamed, M.G., Maiyalagan, T., 2020. Ceram. Int. 46, 6222–6233.
Ramesh, S., Yadav, H.M., Karuppasamy, K., Vikraman, D., Kim, H.-S., Kim, J.-H., Kim, H. S., 2019. J. Mater. Res. Technol. 8, 4227–4238.
Sahoo, S., Pazhamalai, P., Krishnamoorthy, K., Kim, S.-J., 2018. Electrochim. Acta 268, 403–410.
Sakthivel, M., Ramaraj, S., Chen, S.-M., K.-C. J. J. o. M. C. A. Ho, 2019. J. Mater. Chem. 7, 12565–12581.
Salunkhe, R.R., Kaneti, Y.V., Yamauchi, Y., 2017. ACS Nano 11, 5293–5308.
Shah, H.U., Wang, F., Javed, M.S., Ahmad, M.A., Saleem, M., Zhan, J., Khan, Z.U.H., Li, Y., 2018a. J. Energy Storage 17, 318–326.
Shah, H.U., Wang, F., Javed, M.S., Saleem, R., Nazir, M.S., Zhan, J., , Z. U. H. Khan, Farooq, M.U., S. J. I. J. E. S. Ali, 2018b. Int. J. Electrochem. Sci. 13, 6426–6435.
Shen, L., Ding, B., Nie, P., Cao, G., Zhang, X.J.A.E.M., 2013. Adv. Energy Mater. 3, 1484–1489.
Tang, H., Yuan, Y., Meng, L., Wang, W., Lu, J., Zeng, Y., Huang, T., Gao, C.J.A.M.T., 2018. Adv. Mater. Technol. 3, 1800074.
Wan, J., Ji, P., Li, B., Xi, Y., Gu, X., Huang, L., He, M., Hu, C.J.C.C., 2022. Chem. Commun. 58, 589–592.
Wang, X., Liu, W.S., Lu, X., Lee, P.S., 2012. J. Mater. Chem. 22, 23114–23119.
Wang, Y., Zhang, Y.-Z., Gao, Y.-Q., Sheng, G., Johan, E.J.N.E., 2020a. Nano Energy 68, 104306.
Wang, J., Wang, J.-G., Qin, X., Wang, Y., You, Z., Liu, H., Shao, M., 2020b. ACS Appl. Mater. Interfaces 12, 34949–34958.
Weng, Y.T., Pan, H.A., Lee, R.C., Huang, T.Y., Chu, Y., Lee, J.F., Sheu, H.S., N. L. J. A. E. M. Wu, 2015. Adv. Energy Mater. 5, 1500772.
Wu, T., Wang, C., Mo, Y., Wang, X., Fan, J., Xu, Q., Min, Y.J. R.a., 2017. RSC Adv. 7, 33591–33599.
Xiao, Z., Fan, L., Xu, B., Zhang, S., Kang, W., Kang, Z., Lin, H., Liu, X., Zhang, S., Sun, D., 2017. ACS Appl. Mater. Interfaces 9, 41827–41836.
Xing, S., Yang, J., Muska, M., Li, H., Yang, Q., 2021. ACS Appl. Mater. Interfaces 13, 22608–22620.
Yang, X., Zhou, B., Wei, Y., Zou, B., 2017a. CrystEngComm 19, 3331–3337.
Yang, X., Zhou, B., Wei, Y., Zou, B.J.C., 2017b. CrystEngComm 19, 3331–3337.
Yumak, T., Bragg, D., Sabolsky, E.M., 2019. Appl. Surf. Sci. 469, 983–993.
Zeng, Y., Lai, Z., Han, Y., Zhang, H., Xie, S., Lu, X.J.A.M., 2018. Adv. Mater. 30, 1802396.
Zhai, Y., Dou, Y., Zhao, D., Fulvio, P.F., Mayes, R.T., Dai, S.J. A.m., 2011. Adv. Mater. 23, 4828–4850.
Zhang, Y., Sun, C., Lu, P., Li, K., Song, S., Xue, D., 2012. CrystEngComm 14, 5892–5897.
Zhang, Y., Xuan, H., Xu, Y., Guo, B., Li, H., Kang, L., Han, P., Wang, D., Du, Y., 2016a. Electrochim. Acta 206, 278–290.
Zhang, Q., Zhao, B., Wang, J., Qu, C., Sun, H., Zhang, K., Liu, M., 2016b. Nano Energy 28, 475–485.
Zhang, Q.Z., Zhang, D., Miao, Z.C., Zhang, X.L., Chou, S.L.J.S., 2018. Small 14, 1702883.
Zhang, M., Yang, D., Li, J., 2020a. Vacuum 178, 109455.
Zhang, M., Xu, Y., Fan, H., Zhao, N., Yan, B., Wang, C., Ma, J., Yadav, A.K., Zhang, W., Du, Z., Zheng, X., Li, M., Dong, G., Wang, W., 2020b. J. Alloys Compd. 826, 154115.
Zhao, Y., Chang, C., Teng, F., Zhao, Y., Chen, G., Shi, R., Waterhouse, G.I., Huang, W., Zhang, T.J.A.E.M., 2017. Adv. Energy Mater. 7, 1700005.
Zhao, X., Mao, L., Cheng, Q., Li, J., Liao, F., Yang, G., Xie, L., Zhao, C., Chen, L., 2020. Chem. Eng. J. 387, 124081.
Zhao, J., Cong, Z., Hu, J., Lu, H., Wang, L., Wang, H., Malyi, O.I., Pu, X., Zhang, Y., Shao, H.J.N.E., 2022. Nano Energy 93, 106893.
Zhu, Y., Huang, C., Li, C., Fan, M., Shu, K., Chen, H.C., 2019. J. Power Sources 412, 559–567.